

## Article

# Enhanced Performance in Si<sub>3</sub>N<sub>4</sub> Ceramics Cutting Tool Materials by Tailoring of Phase Composition and Hot-Pressing Temperature

Shuai Guo <sup>1,2</sup>, Fusheng Zhu <sup>1</sup>, Zhimeng Xiu <sup>1</sup>, Mu Zhang <sup>1,2,\*</sup> and Xudong Sun <sup>1,2,\*</sup>

<sup>1</sup> Key Laboratory for Anisotropy and Texture of Materials (Ministry of Education), School of Materials Science and Engineering, Northeastern University, Shenyang 110819, China

<sup>2</sup> Foshan Graduate School of Innovation, Northeastern University, Foshan 528311, China

\* Correspondence: zhangm@mail.neu.edu.cn (M.Z.); xdsun@mail.neu.edu.cn (X.S.)

**Abstract:** In this study, a type of micro-nano Si<sub>3</sub>N<sub>4</sub> matrix ceramic cutting tool material was successfully prepared by controlling the addition amount of TiC<sub>0.7</sub>N<sub>0.3</sub> and the hot-pressing sintering temperature. The effects of different volume fractions of TiC<sub>0.7</sub>N<sub>0.3</sub> on the microstructure, mechanical properties, particle size distribution, and relative density of Si<sub>3</sub>N<sub>4</sub> ceramic tools at the same temperature were investigated. The results show that the addition of TiC<sub>0.7</sub>N<sub>0.3</sub> makes the β-Si<sub>3</sub>N<sub>4</sub> grains with different diameters and aspect ratios interlaced and tightly bonded, thus achieving the strengthening and toughening effects. In addition, the effects of different hot-press sintering temperatures on the properties of Si<sub>3</sub>N<sub>4</sub> ceramic tool materials were studied. It was concluded that the density of the material increased with the increase of the hot-pressing temperature. The relative density, flexural strength, and fracture toughness of the samples with 1 vol% TiC<sub>0.7</sub>N<sub>0.3</sub> added at 1750 °C and 30 MPa pressure reached 99.22%, 993 MPa, and 9.81 MPa·m<sup>1/2</sup>, respectively.

**Keywords:** Si<sub>3</sub>N<sub>4</sub>; ceramic cutting tool; hot-pressing sintering; TiC<sub>0.7</sub>N<sub>0.3</sub>; self-toughening



**Citation:** Guo, S.; Zhu, F.; Xiu, Z.; Zhang, M.; Sun, X. Enhanced Performance in Si<sub>3</sub>N<sub>4</sub> Ceramics Cutting Tool Materials by Tailoring of Phase Composition and Hot-Pressing Temperature. *Coatings* **2023**, *13*, 475. <https://doi.org/10.3390/coatings13020475>

Academic Editor: Ben Beake

Received: 16 January 2023

Revised: 11 February 2023

Accepted: 14 February 2023

Published: 20 February 2023



**Copyright:** © 2023 by the authors. Licensee MDPI, Basel, Switzerland. This article is an open access article distributed under the terms and conditions of the Creative Commons Attribution (CC BY) license (<https://creativecommons.org/licenses/by/4.0/>).

## 1. Introduction

With the development of modern manufacturing technology, the use of various new difficult-to-machine materials is increasing, such as iron-based, nickel-based, cobalt-based, titanium-based superalloys, ultra-high strength steel, and high wear-resistant cast iron. Therefore, the cutting and machining of such materials are becoming increasingly important. However, with the current use of traditional hard alloy or high-speed steel and other tool materials to process, tool life is very low or even impossible to process. This prompted people to study and manufacture suitable-for-processing engineering materials for use as tool materials. Because of the outstanding performance of high-toughness ceramic tools, ceramic tools are considered to be the most prominent and widely useful option. In modern machining, ceramic materials have become the most promising utility tool materials due to their excellent heat resistance, high-temperature oxidation resistance, high hardness, and wear resistance [1–5].

Although ceramics cutting tools play an increasingly important role in cutting difficult-to-machine materials, ceramics cutting tools suffer from relatively low fracture toughness and ductility due to the inherent brittleness of ceramic materials [6]. Therefore, some scholars have focused their research on improving the fracture toughness of conventional ceramic tool materials to meet the requirements of high-speed precision cutting processing. Some researchers choose to prepare a coating (cBN coating, [7] TiAlN coating, [8,9] WS<sub>2</sub>/Zr soft-coating [10]) on the surface of the ceramic tool to achieve the purpose of improving the tool life, study the wear mechanism of the tool during cutting, and prepare a composite ceramic tool with good performance. These coatings can effectively prevent the internal

ceramic material from being corroded, thereby increasing the service life of the tool. Miłojczyk et al. [11] studied a new selective exchange worn cutting edge (SEWCE) scheme, which achieved the effect of reducing tool cost. Wang et al. [12] fabricated  $\text{Si}_3\text{N}_4$  ceramic cutting tools with high fracture toughness by introducing tungsten particles and changing nitrogen pressure. Lucchini et al. [13] found that although the  $\text{Al}_2\text{O}_3/\text{Mo}$  composite increases the toughness of the ceramic cutting tool, there is a performance defect in some material cutting due to the too-low adhesion between the  $\text{Al}_2\text{O}_3$  matrix and the Mo dispersion. TiCN-based materials have the characteristics of high hardness and high melting point, so they are also widely used in various metal-based ceramic materials [14–17]. It has been reported that adding 10–30 wt.% coarse TiCN to ultrafine TiCN metal-based ceramics can significantly improve the fracture toughness and strength of the material [18]. In the past, there were very few studies on TiCN-toughened silicon nitride ceramic materials. The  $\text{TiC}_{0.7}\text{N}_{0.3}$  used in this experiment is a continuous solid solution formed by TiC and TiN, both of which have high hardness and high melting points. Most academic research focuses on the performance improvement of  $\text{Si}_3\text{N}_4$  by TiC or TiN [4,10,19–21], while  $\text{TiC}_{0.7}\text{N}_{0.3}$  is mostly used to improve the performance of other ceramic materials.

In this study,  $\text{Si}_3\text{N}_4$ -based ceramic materials with good overall performance were prepared from two commercial ultrafine  $\text{Si}_3\text{N}_4$  powders by controlling the addition of  $\text{TiC}_{0.7}\text{N}_{0.3}$  and different sintering temperatures. In addition, the chemical composition, microstructure, and micro-interface of the  $\text{Si}_3\text{N}_4$ -based ceramics were characterized, and the mechanical properties of the ceramics were measured. In addition, the bimodal particle size distribution phenomenon and the self-toughening principle of  $\beta\text{-Si}_3\text{N}_4$  are discussed.

## 2. Experimental Procedures

Two sizes of commercial  $\alpha\text{-Si}_3\text{N}_4$  powders ( $\alpha > 92.5$  wt.%,  $D_{50} = 0.8$   $\mu\text{m}$  and  $D_{50} = 0.35$   $\mu\text{m}$ , oxygen content = 1.20 wt.%, Shanghai Ansame Fine Ceramics Co., Ltd., Shanghai, China) were used.  $\text{Al}_2\text{O}_3$  (purity  $\geq 99.9$  wt.%, Shanghai Aladdin Biochemical Technology Co., Ltd., Shanghai, China),  $\text{Y}_2\text{O}_3$  (purity  $\geq 99.5$  wt.%, Shanghai Aladdin Biochemical Technology Co., Ltd., Shanghai, China), and  $\text{TiC}_{0.7}\text{N}_{0.3}$  ultrafine powder (purity  $\geq 98\%$ ,  $D_{50} = 200$  nm, Shijiazhuang Huatai Ceramic Materials Factory, Shijiazhuang, China) were used as raw materials. The 0.8  $\mu\text{m}$   $\text{Si}_3\text{N}_4$  powder was marked as  $\text{Si}_3\text{N}_4\text{-80}$ , and the 0.35  $\mu\text{m}$   $\text{Si}_3\text{N}_4$  powder was marked as  $\text{Si}_3\text{N}_4\text{-35}$ . In this experiment, a combined  $\text{Y}_2\text{O}_3\text{-Al}_2\text{O}_3$  sintering aid was selected, and the Si-Al-O-N and Y-Si-O-N liquid phases formed during the sintering process allowed for more than adequate sintering of the  $\text{Si}_3\text{N}_4$  [22,23]. The starting composition was determined to be  $\text{Si}_3\text{N}_4\text{-80}:\text{Si}_3\text{N}_4\text{-35}:\text{Y}_2\text{O}_3:\text{Al}_2\text{O}_3 = 87:5:6:2$  by mass ratio, and the powder was weighed and planetary ground in ethanol at a speed of 300 rpm using  $\text{Si}_3\text{N}_4$  balls for 10 h. After the planetary milling, the mixed slurry was poured out and placed in an oven for drying at a drying temperature of 60  $^\circ\text{C}$ . The ground and dried powder was passed through an 80-mesh sieve and recorded as the initial powder SN. According to different  $\text{TiC}_{0.7}\text{N}_{0.3}$  contents and different hot-pressing temperatures, it is divided into five experimental schemes, SN1, SN2, SN3, SN4, and SN5, for hot-pressing sintering at 30 MPa pressure, as shown in Table 1.

**Table 1.** Starting powder composition (vol%) and sintering parameter.

Sample	SN	$\text{TiC}_{0.7}\text{N}_{0.3}$	Temperature ( $^\circ\text{C}$ )
SN1	100	/	1650
SN2	99	1	1650
SN3	97	3	1650
SN4	99	1	1700
SN5	99	1	1750

The samples obtained by sintering were cut into several standard samples of 40 mm  $\times$  5 mm  $\times$  6 mm with a diamond cutter, and the standard samples were polished and ground until the surface was mirror-like for various performance tests. Relative densities of  $\text{Si}_3\text{N}_4$  tool material were evaluated by the Archimedes method. Phase characteriza-

tion was performed by X-ray diffraction (XRD; PW3040/60, Panalytical Ltd, Netherlands, The Netherlands). Backscatter observation and energy spectrum analysis were performed on the polished surface of the specimen using a scanning electron microscope of SSX-550 (Shimadzu, Kyoto, Japan). The Vickers hardness of the material was measured with a 450SVD™ Vickers hardness tester (Walbert Measuring Instruments (Shanghai) Co., Ltd., Shanghai, China), the indentation load was 10 Kg, and the diamond indenter was loaded on the surface of the sample for 15 s. The single-edge notched beam (SENB) method was used to test the fracture toughness of the material. The strength of the material was measured using the three-point flexural strength method. The surface of the ground and polished sample strip was tested on a SANS computer-controlled electronic universal testing machine (Shenzhen Xinsansi Material Testing Co., Ltd., Shenzhen, China).

### 3. Results and Discussion

Figure 1 shows the morphology of the SN2 mixed powder. In the SN2 composite powder of various raw materials mixed and dispersed by ball milling, the particles are separated from each other, the small particles are dispersed between the large particles, and there is no agglomeration between the large and small particles. This shows that the composite powder after dispersion treatment is evenly mixed and has good dispersibility, which is beneficial for the subsequent experiments.

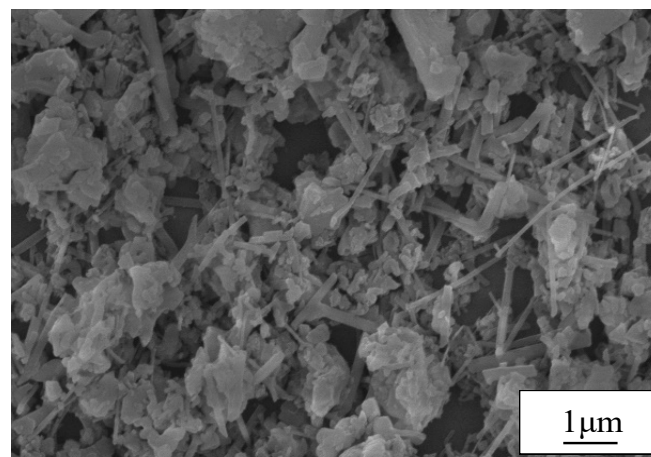
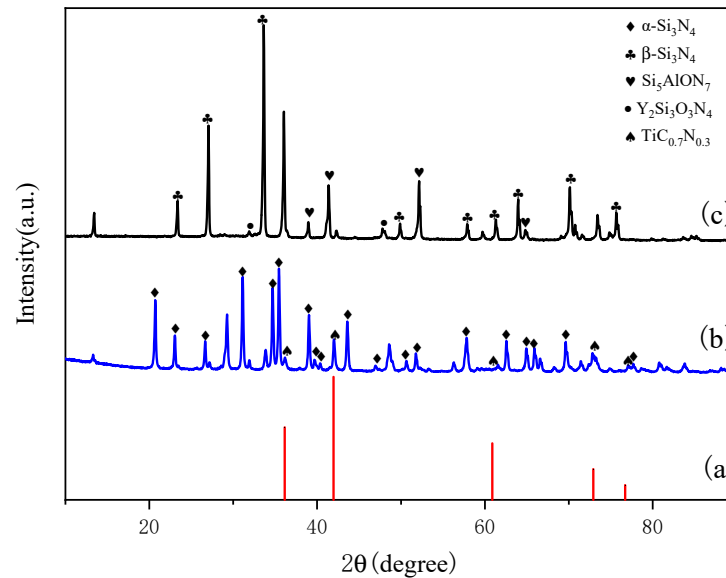


Figure 1. SEM image of SN2 sample powder before hot-pressing sintering.

X-ray diffraction (XRD) phase analysis was performed on the pre-compact body and sintered body before and after hot-pressing sintering, respectively, to determine the phase change before and after sintering, as shown in Figure 2. Based on the analysis of the XRD pattern, it can be seen that the  $\text{Si}_3\text{N}_4$  before sintering is mainly  $\alpha\text{-Si}_3\text{N}_4$ , and there is only  $\beta\text{-Si}_3\text{N}_4$  remaining in the sample after sintering, indicating that during the sintering process, the  $\alpha\text{-Si}_3\text{N}_4$  in the initial powder is all converted into columnar  $\beta\text{-Si}_3\text{N}_4$  [24,25]. In addition, oxygen-containing sintering aids react with surface  $\text{SiO}_2$  and  $\text{Si}_3\text{N}_4$  to form a liquid phase of oxynitride at a high temperature. That is, during the high-temperature sintering process of  $\text{Si}_3\text{N}_4$ ,  $\text{Al}_2\text{O}_3$  enters the  $\text{Si}_3\text{N}_4$  crystal, and  $\text{Al}^{3+}$  and  $\text{O}^{2-}$  ions replace part of the  $\text{Si}^{4+}$  and  $\text{N}^{3-}$  ions in the  $\text{Si}_3\text{N}_4$  lattice, respectively. This forms the Si-Al-O-N (which is  $\beta$ -sialon) phase,  $\text{Y}_2\text{O}_3$  becomes Y-N apatite, and the Y-Si-O-N phase appears. The resulting liquid phase can provide a solvent for bond breaking, reconstruction, and phase transition; phase transition usually occurs only at the solid-liquid phase contact because the sintering and densification of  $\text{Si}_3\text{N}_4$  are affected by the solubility and viscosity of the liquid phase [26–28]. During the phase transition, the unstable and easily soluble  $\alpha\text{-Si}_3\text{N}_4$  dissolves into the liquid phase, while the stable and insoluble  $\beta$  phase is precipitated, and this liquid phase becomes the grain boundary phase when cooled. It can be seen from XRD (Figure 2) that the  $\text{TiC}_{0.7}\text{N}_{0.3}$  phase exists before and after sintering. Therefore, it can be

inferred that  $\text{TiC}_{0.7}\text{N}_{0.3}$  does not undergo phase transformation during the experiment but is uniformly dispersed in the  $\text{Si}_3\text{N}_4$  matrix.



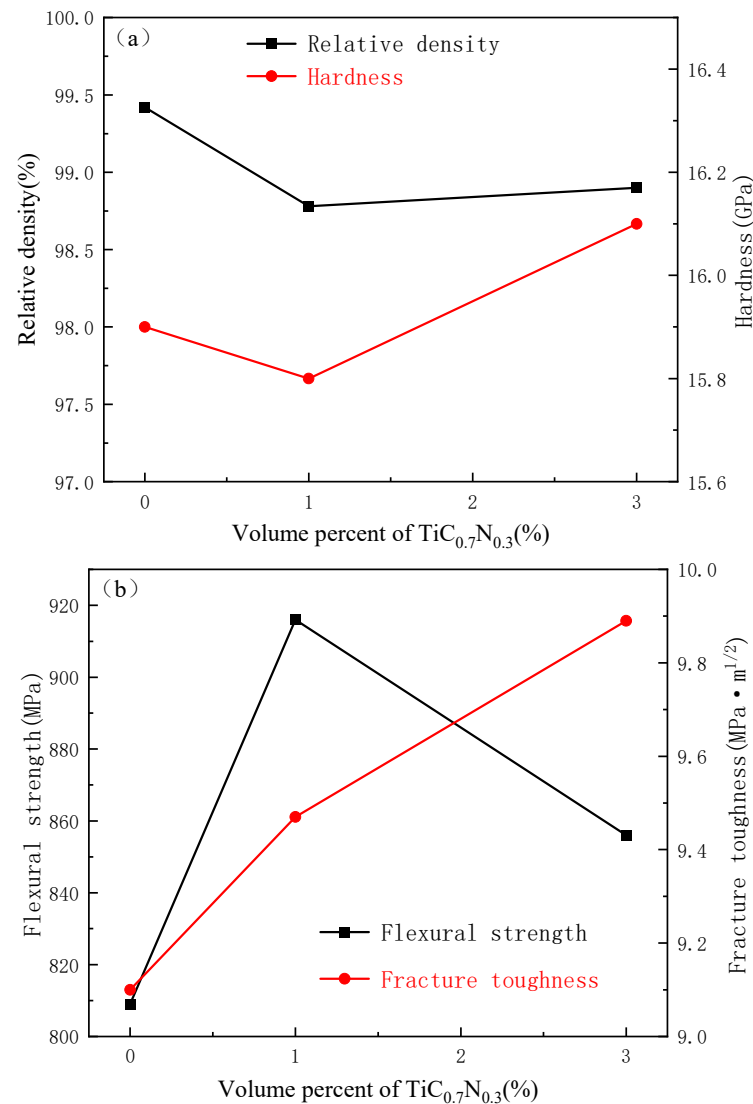
**Figure 2.** X-ray diffraction (XRD) patterns of SN2 samples before and after sintering at 1650 °C for 1 h: (a) Standard data for  $\text{TiC}_{0.7}\text{N}_{0.3}$  (PDF#42-1489); (b) Sample before sintering; (c) Sample after sintering.

Table 2 presents the mechanical properties of materials with different  $\text{TiC}_{0.7}\text{N}_{0.3}$  additions. Figure 3 shows the relationship between the relative density, hardness, flexural strength, fracture toughness of the material, and the amount of  $\text{TiC}_{0.7}\text{N}_{0.3}$  added. It can be seen from Figure 3a that with the increase of the addition amount of the second phase  $\text{TiC}_{0.7}\text{N}_{0.3}$ , the relative density of the material has a downward trend. However, the relative density is more than 98%, which can be regarded as densification at the same time, and the overall hardness has an increasing trend. This is because  $\text{TiC}_{0.7}\text{N}_{0.3}$  has the characteristics of high hardness [29,30]. In the meantime, the addition of  $\text{TiC}_{0.7}\text{N}_{0.3}$  is equivalent to adding a hard second phase, so it can be expected that when the addition amount continues to increase, the hardness of the material will further increase.

Furthermore, adding 1 vol% of  $\text{TiC}_{0.7}\text{N}_{0.3}$  can significantly improve the flexural strength of the material, but when the addition is 3 vol%, it decreases significantly. It can be seen from Figure 3b that the fracture toughness increases gradually with the increase in the addition amount. The toughening effect of  $\text{TiC}_{0.7}\text{N}_{0.3}$  on the matrix material is mainly due to the difference in thermal expansion coefficient and elastic modulus between the  $\text{Si}_3\text{N}_4$  matrix and the dispersed phase particles of  $\text{TiC}_{0.7}\text{N}_{0.3}$ . In the process of material preparation, when sintering and cooling, local residual stress will inevitably be generated. When the residual stress is greater than a certain value, microcracks will be generated. During the propagation of the main crack, the energy required for the propagation of the main crack is consumed by microcracks, thereby improving the fracture toughness of the material. Among the four performance indicators of the material, under the premise that the relative density, Vickers hardness, and fracture toughness do not change much, the flexural strength of the material added with 1 vol%  $\text{TiC}_{0.7}\text{N}_{0.3}$  is the best. Therefore, among the three samples with different compositions, the best comprehensive performance is the sample with the  $\text{TiC}_{0.7}\text{N}_{0.3}$  addition of 1 vol%.

**Table 2.** Effect of  $\text{TiC}_{0.7}\text{N}_{0.3}$  content on the mechanical properties of materials.

Sample	Relative Density (%)	Bending Strength (MPa)	Fracture Toughness ( $\text{MPa}\cdot\text{m}^{1/2}$ )	Vickers Hardness (GPa)
SN1	99.42	809	9.10	15.9
SN2	98.78	916	9.47	15.8
SN3	98.90	856	9.89	16.1



**Figure 3.** The effect of different volume fractions of  $\text{TiC}_{0.7}\text{N}_{0.3}$  in SN1, SN2, and SN3 on the properties: (a) Relative density and Vickers hardness; (b) Flexural strength and fracture toughness.

Figure 4 is the backscattered photos of the polished surface of the sample without and with 1 vol% and 3 vol%  $\text{TiC}_{0.7}\text{N}_{0.3}$  added. It can be seen in Figure 4a–c that the black parts are distributed in stripes of different sizes, and the white areas are evenly distributed. With the increase of  $\text{TiC}_{0.7}\text{N}_{0.3}$  addition, the size of the black strips gradually decreased. The uniform distribution of the black and white areas indicates that the powders are well-mixed and have no serious agglomeration. Figure 5a,b is the energy spectrum (EDS) analysis of points A and B in Figure 4c, respectively. Combined with the XRD phase analysis of the sintered body (Figure 2c), it can be seen that point A, that is, the white area in the figure, is mainly the Y-Si-O-N phase, and there is also a small amount of the Si-Al-O-N phase. Point B, which is the black area in the figure, is mainly the  $\beta\text{-Si}_3\text{N}_4$  phase and also has a small amount of Al, indicating that it also contains a small amount of the Si-Al-O-N phase. Since the addition of  $\text{TiC}_{0.7}\text{N}_{0.3}$  is very small, the Ti is not obvious in the energy spectrum. As a result, it is difficult to determine whether it is distributed at the grain boundaries of  $\beta\text{-Si}_3\text{N}_4$  or involved in the nucleation of  $\beta\text{-Si}_3\text{N}_4$  and located at its crystal lattice.

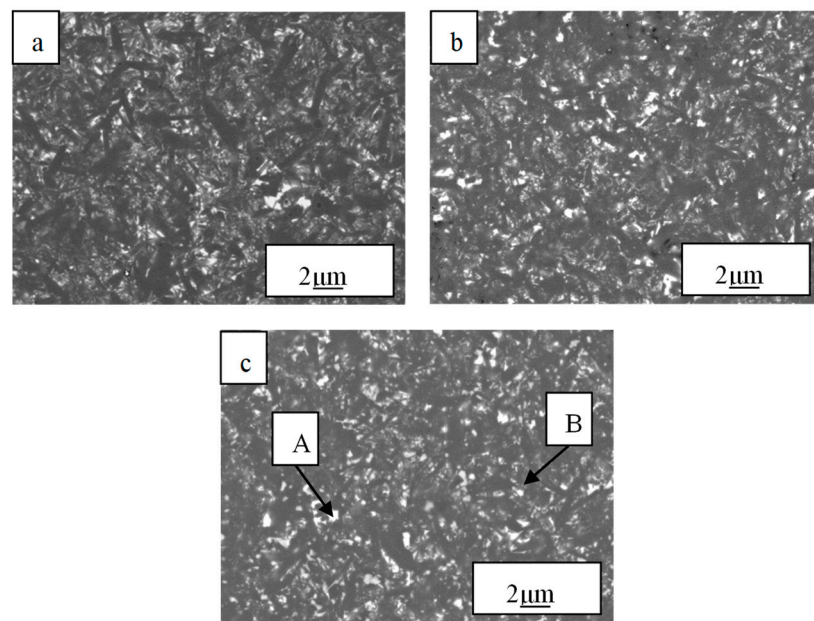


**Figure 4.** Backscattering photos of the polished surface of samples with different  $\text{TiC}_{0.7}\text{N}_{0.3}$  contents: (a) without  $\text{TiC}_{0.7}\text{N}_{0.3}$ ; (b) 1 vol%  $\text{TiC}_{0.7}\text{N}_{0.3}$ ; (c) 3 vol%  $\text{TiC}_{0.7}\text{N}_{0.3}$ .

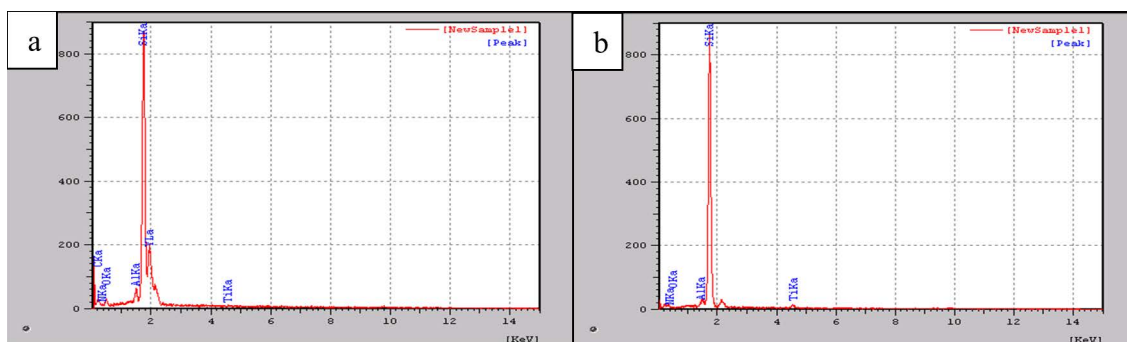


**Figure 5.** Energy spectrum analysis (a) Point A in Figure 4c; (b) Point B in Figure 4c.

It can be seen from Figure 6 that with the change in the addition amount of  $\text{TiC}_{0.7}\text{N}_{0.3}$ , the microstructure of the material has undergone a relatively obvious change. The  $\text{Si}_3\text{N}_4$  matrix in the sintered body is all long columnar  $\beta\text{-Si}_3\text{N}_4$  grains with different diameters and aspect ratios interlaced with each other, and the fractures are rough. From the fracture morphology of the material (Figure 6a–c), it can be clearly seen that the holes and part of the grain section are left by the grain pulling out. This indicates that the fracture mode is a combination of intergranular fracture and transgranular fracture. The long columnar  $\beta\text{-Si}_3\text{N}_4$  has the effect of strengthening and toughening similar to fibers and whiskers. This is the self-toughening of  $\text{Si}_3\text{N}_4$ , and it is also an important reason why the flexural strength and fracture toughness of  $\text{Si}_3\text{N}_4$ -based ceramic tool materials are higher than other tool materials. At the same time, a small amount of  $\beta\text{-Si}_3\text{N}_4$  in the raw material exists in the form of seed crystals, and self-toughening  $\text{Si}_3\text{N}_4$  ceramics can also be synthesized [31,32]. In addition, a small number of irregularly shaped and deep holes can be seen from the fracture of the material. These are the pores inside the material, indicating that the density of the material is not enough, especially the pores in Figure 6b are more obvious, and the number of pores is slightly more than the other two. This also corresponds to the lowest relative density of the sample added with 1 vol%  $\text{TiC}_{0.7}\text{N}_{0.3}$  measured earlier. It can also be seen from Figure 6 that with the increase of  $\text{TiC}_{0.7}\text{N}_{0.3}$  addition amount, the average grain size gradually decreases.

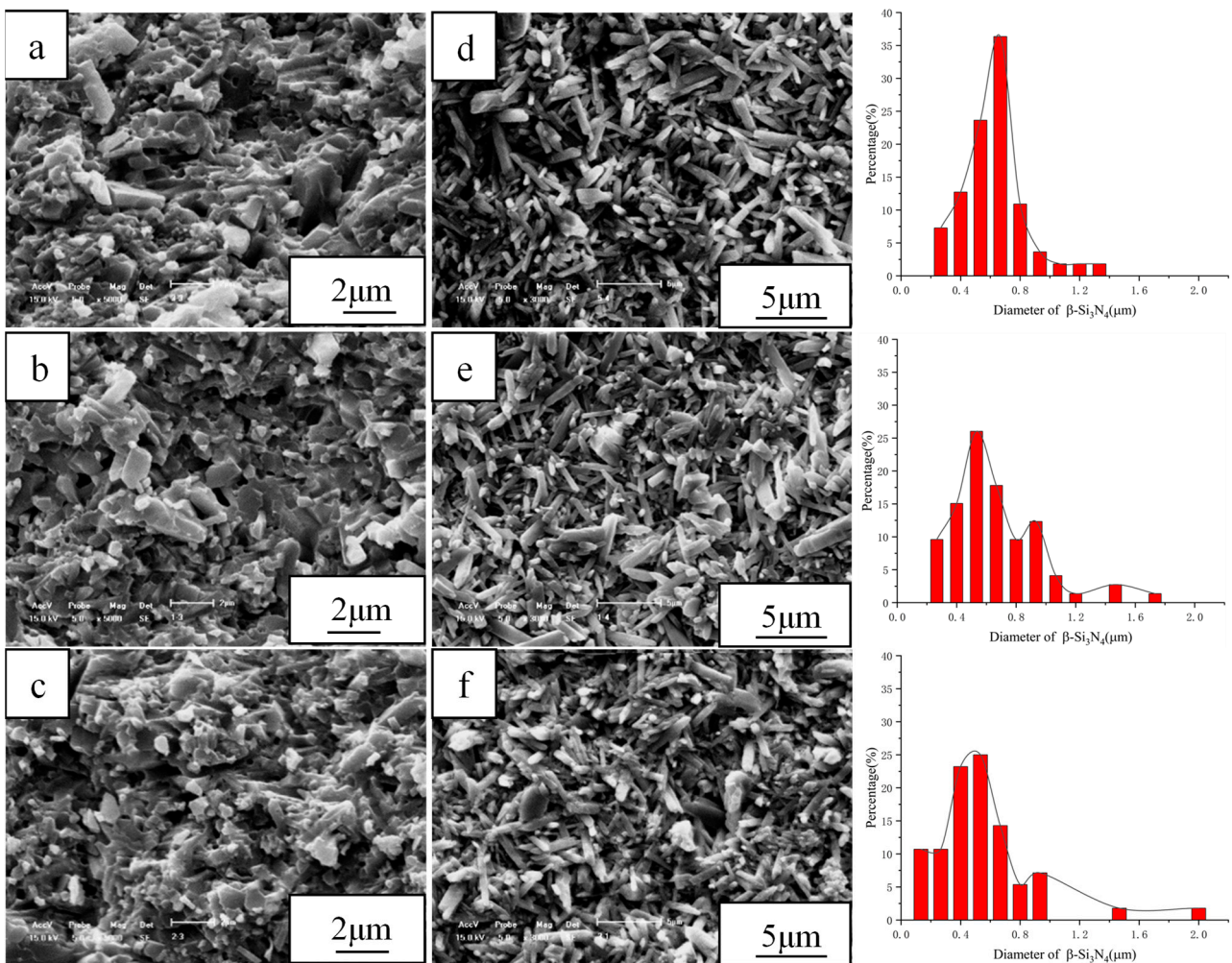


**Figure 6.** (a–c) are the fracture scan photos of no addition, the addition of 1 vol%, and the addition of 3 vol%  $\text{TiC}_{0.7}\text{N}_{0.3}$ , respectively; (d–f) are the scanning photos of the corroded surface without adding, adding 1 vol%, and adding 3 vol%  $\text{TiC}_{0.7}\text{N}_{0.3}$ , respectively. On the right are the diameter distributions of the three corresponding  $\beta\text{-Si}_3\text{N}_4$  grains.

It can be seen from Figure 6d–f of the corroded surface topography that the grains without  $\text{TiC}_{0.7}\text{N}_{0.3}$  are more uniform and have little difference in size. After adding a small amount of  $\text{TiC}_{0.7}\text{N}_{0.3}$ , due to the pinning effect of the second phase particles, the growth of part of the grains is prevented so that the diameter and aspect ratio range of the overall grains increases. Small grains are embedded between large grains, and the structure is more tightly packed. This is also the reason why the flexural strength increases after adding 1 vol%  $\text{TiC}_{0.7}\text{N}_{0.3}$ . When the addition amount is 3 vol%, the number of small grains is too large, which weakens the self-toughening effect of  $\text{Si}_3\text{N}_4$ . Therefore, the flexural strength starts to decrease again while the fracture toughness continues to increase, which is still due to the difference in thermal expansion coefficient and elastic modulus between the  $\text{Si}_3\text{N}_4$  matrix and the dispersed phase particles of  $\text{TiC}_{0.7}\text{N}_{0.3}$ .

It can be clearly seen from the particle size distribution diagram on the right that the diameter of  $\beta\text{-Si}_3\text{N}_4$  grains in the sample without  $\text{TiC}_{0.7}\text{N}_{0.3}$  is concentrated between 0.4 and 0.8  $\mu\text{m}$ . After adding 1 vol%  $\text{TiC}_{0.7}\text{N}_{0.3}$ , the diameters of  $\beta\text{-Si}_3\text{N}_4$  grains are concentrated between 0.3 and 1  $\mu\text{m}$ . After adding 3 vol%  $\text{TiC}_{0.7}\text{N}_{0.3}$ , the diameters of  $\beta\text{-Si}_3\text{N}_4$  grains are concentrated between 0.1 and 0.65  $\mu\text{m}$ . It shows that the addition of  $\text{TiC}_{0.7}\text{N}_{0.3}$  reduces the diameter of some  $\beta\text{-Si}_3\text{N}_4$  grains in the sample and increases the diameter distribution range. It can also be seen that the diameter of  $\beta\text{-Si}_3\text{N}_4$  grains has a bimodal distribution, especially the bimodal distribution of the 1 vol%  $\text{TiC}_{0.7}\text{N}_{0.3}$  sample

is more obvious. At the same time, when the grain size of  $\beta$ - $\text{Si}_3\text{N}_4$  in the  $\text{Si}_3\text{N}_4$  matrix presents a bimodal distribution, its mechanical properties are greatly improved [33–35]. This is also an important reason for the improvement of the mechanical properties of the material after adding a small amount of  $\text{TiC}_{0.7}\text{N}_{0.3}$ .

The above discussion can be concluded that the addition of  $\text{TiC}_{0.7}\text{N}_{0.3}$  has a certain effect on the relative density and hardness of ceramic tool materials. However,  $\text{TiC}_{0.7}\text{N}_{0.3}$  exists as a hard second phase in the  $\text{Si}_3\text{N}_4$  grain boundary, and the second phase particles act as pegging. When the addition amount is 1 vol%, the  $\beta$ - $\text{Si}_3\text{N}_4$  grains have an overall bimodal structure. Different diameters of  $\beta$ - $\text{Si}_3\text{N}_4$  are interlaced with each other, which makes the flexural strength of ceramic tools much higher.

In the process of hot-pressing sintering, the influence of hot-pressing temperature on the properties of materials is also very obvious. The addition of sintering aids can reduce the sintering temperature, and the optimal sintering temperature of different sintering aid combinations is also different. It can be seen from Figure 2c that the mixed powder with 1 vol%  $\text{TiC}_{0.7}\text{N}_{0.3}$  that was hot-pressed and sintered at a sintering temperature of 1650 °C for one hour, the  $\alpha \rightarrow \beta$  phase transition was complete. Therefore, when the sintering temperature increased to 1700 and 1750 °C, the phase composition of SN2, SN4, and SN5 samples did not change after sintering. It was still the four phases of  $\beta$ - $\text{Si}_3\text{N}_4$ , Si-Al-O-N (which is  $\beta$ -sialon), Y-Si-O-N, and  $\text{TiC}_{0.7}\text{N}_{0.3}$ . In XRD images (Figure 7), the difference between the three images is only the difference in peak strength.

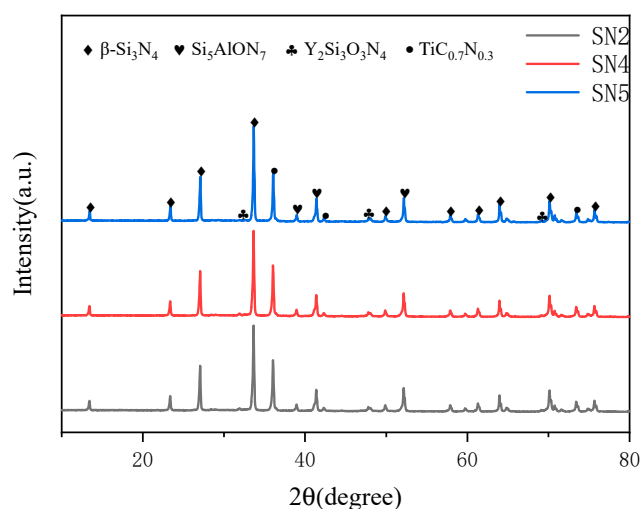


**Figure 7.** XRD patterns of samples at different hot-pressing temperatures: The sintering temperatures of SN2, SN4, and SN5 samples were 1650, 1700, and 1750 °C, respectively.

Table 3 presents the mechanical properties of the materials prepared at different hot-pressing sintering temperatures. Figure 8 shows the relationship between the relative density, hardness, flexural strength, fracture toughness of the material, and hot-pressing sintering temperature. It can be seen from Figure 8 that with the increase of hot-pressing temperature, the relative density of the material increases gradually, indicating that increasing the hot-pressing sintering temperature can promote the densification of the material. The Vickers hardness of the material had almost no change, indicating that the hardness of the material is mainly affected by its composition and phase, and is little affected by the hot-pressing temperature. In addition, the flexural strength and fracture toughness of the material increased significantly with the increase in hot-pressing temperature, which may be related to the increase in the material density or the change in grain size, which can be verified by the microstructure and morphology. Some researchers claim that the  $\alpha$ - $\text{Si}_3\text{N}_4$  powder can be completely densified under the temperature of about 1850 °C and the pressure hot-pressing of 23 MPa [36]. However, our temperature has not reached 1850 °C at present, so by increasing the hot-pressing sintering temperature, the comprehensive performance of the  $\text{Si}_3\text{N}_4$ -based ceramic tool material can be further improved.

**Table 3.** Effect of hot-pressing temperature on the mechanical properties of materials.

Sample	Relative Density (%)	Bending Strength (MPa)	Fracture Toughness (MPa·m <sup>1/2</sup> )	Vickers Hardness (GPa)
SN2	98.78	916	9.47	15.8
SN4	99.04	961	9.95	15.9
SN5	99.22	993	9.81	15.9

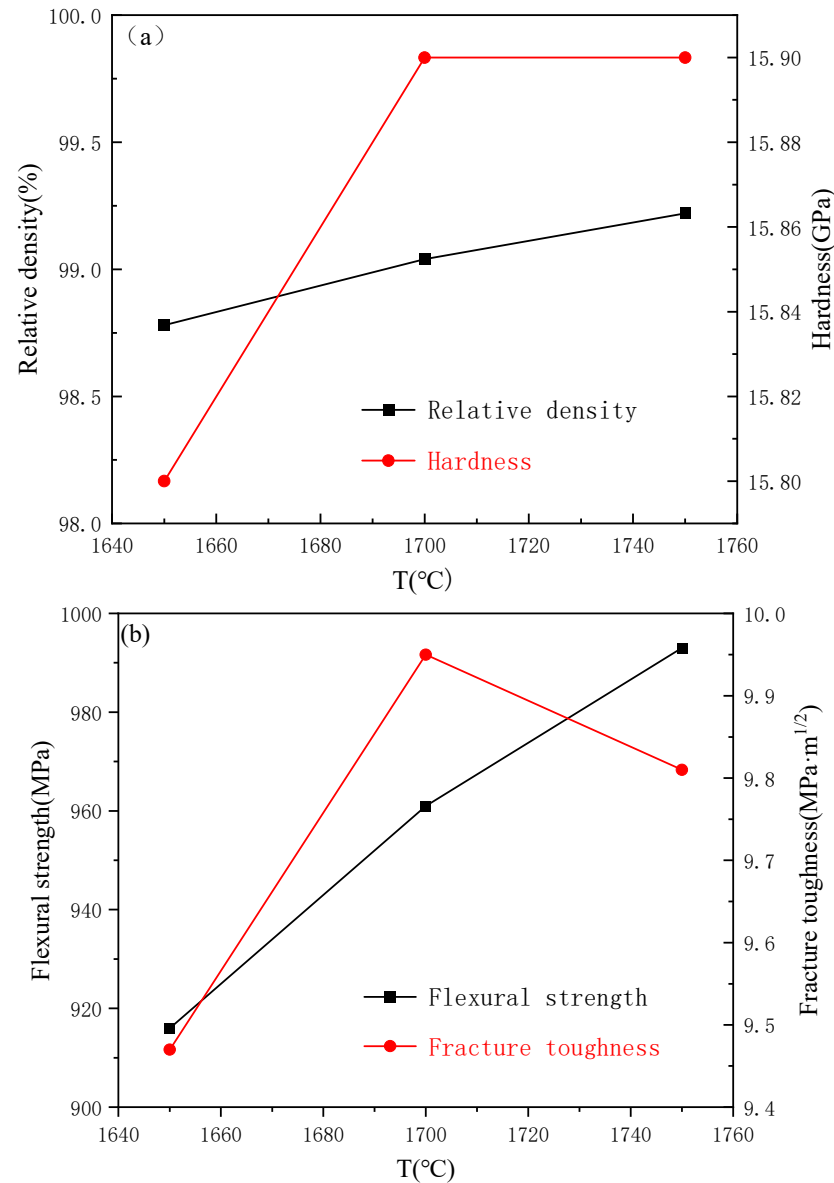
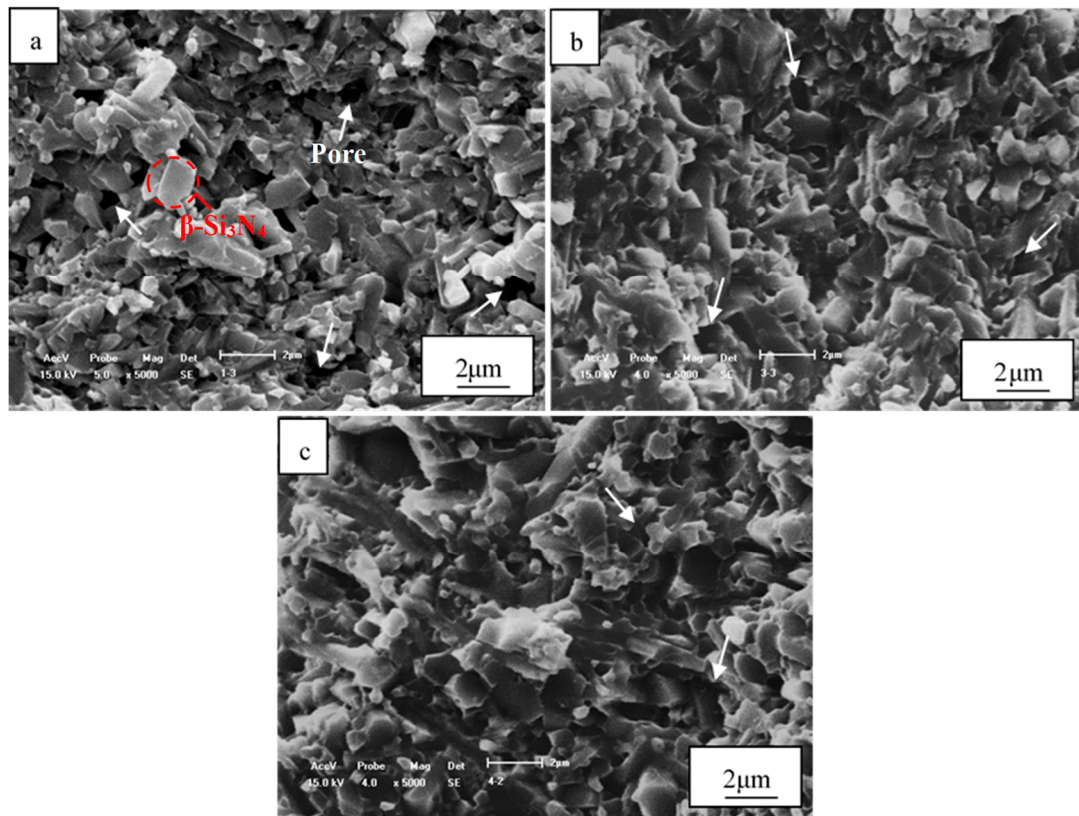
**Figure 8.** Comparison of performance parameters of SN2, SN4, and SN5 samples at different sintering temperatures: (a) Relative density and Vickers hardness; (b) Flexural strength and fracture toughness.

Figure 9 shows the scanned photographs of the fracture cross-sections at three hot pressing temperatures. When sintered at 1650 °C, the  $\beta$ -Si<sub>3</sub>N<sub>4</sub> seeds in the raw material grow through the Ostwald maturation mechanism. Due to the relatively low sintering temperature, the overall grain radius is relatively small, and there are many pores at the grain boundary. The TiC<sub>0.7</sub>N<sub>0.3</sub> in the raw material is uniformly dispersed in the Si<sub>3</sub>N<sub>4</sub> matrix. Because its thermal expansion coefficient and elastic modulus are different from those of Si<sub>3</sub>N<sub>4</sub>,  $\beta$ -Si<sub>3</sub>N<sub>4</sub> grains with different diameters and different aspect ratios are interlaced and tightly combined with each other during the sintering process to achieve the effect of reinforcement and toughening.



**Figure 9.** The fracture surfaces SEM of SN2, SN4, and SN5 samples sintered at different temperatures: (a) 1650 °C; (b) 1700 °C; (c) 1750 °C.

In the sintering process, there are two main factors affecting the crystal growth, one is the diffusion rate of solute atoms, and the other is the deposition rate of solute atoms at the particle-matrix interface [37]. In this experiment, with the increase of temperature under the same conditions, the diffusion rate of solute atoms increases greatly, making the grain size of  $\beta$ - $\text{Si}_3\text{N}_4$  larger. At the same time, the density of the material increases, and the porosity defect decreases so that the mechanical properties such as flexural strength, fracture toughness, and hardness are improved.

At the same time, we can also draw from Figure 9, with the change of hot-pressing sintering temperature, the intrinsic reasons for the change of mechanical properties of materials. With the increase of hot-pressing sintering temperature, the phenomenon of grain pull-out during fracture becomes more and more obvious, and the fracture is rougher; that is, the holes left after grain pulling out are larger and deeper. This indicates that the diameter and length of the grains increased. Due to the existence of rod-like  $\beta$ - $\text{Si}_3\text{N}_4$ , crack deflection and bridging occur during crack propagation, which increases the crack deflection angle, consumes more energy, and inhibits crack propagation [26,35]. Furthermore, the larger the rod size, the better the effect. The  $\beta$ - $\text{Si}_3\text{N}_4$  particles at 1750 °C are larger than other samples, so the performance is better. It may be that the increase in temperature makes a large amount of liquid phase to be formed at the grain boundary during the sintering process, which increases the crystal phase transformation rate and makes the particle diameter of  $\beta$ - $\text{Si}_3\text{N}_4$  larger. Compared with those shown in Figure 9a,b, the fracture surface (Figure 9c) seems to be denser, and the number of irregularly-shaped deeper pores at the fracture is significantly reduced. This basically conforms to the relative density variation trend of samples at different temperatures shown in Table 3. Therefore, increasing the sintering temperature is helpful to improve the flexural strength and fracture toughness of the samples.

Figure 10 is the distribution curve of the aspect ratio of  $\beta$ - $\text{Si}_3\text{N}_4$  grains in samples with hot-pressing sintering temperatures of 1650, 1700, and 1750 °C. It can be seen that with the increase in hot-pressing temperature, the aspect ratio of  $\beta$ - $\text{Si}_3\text{N}_4$  grains increases significantly. This makes the inter-grain interleaving of  $\text{Si}_3\text{N}_4$  more complex so that the overall mechanical properties are relatively high. This is the same as the previous experimental results. At the same time, the mechanical properties still show an increasing trend as the temperature continues to increase. The increase in grain diameter and aspect ratio enhances the self-toughening effect of the material and improves the overall performance [38].

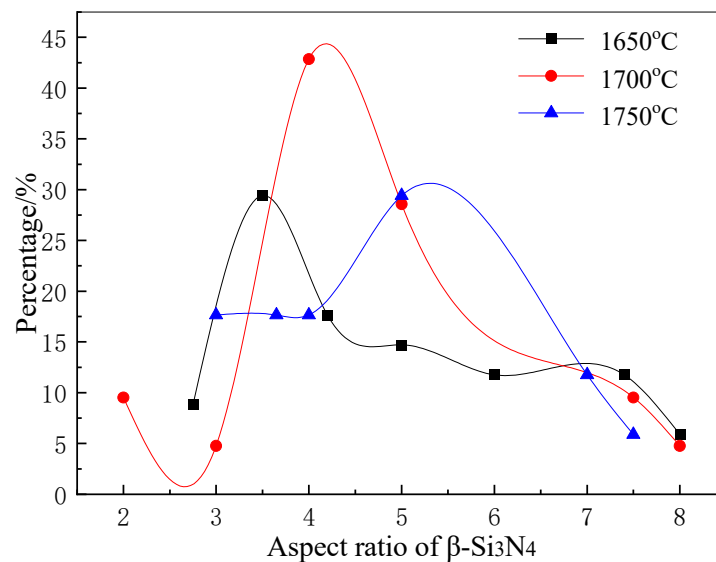


**Figure 10.** The distribution curves of the aspect ratio of  $\beta$ - $\text{Si}_3\text{N}_4$  grains in SN2, SN4, and SN5 at different hot-pressing temperatures.

#### 4. Conclusions

In this study, the mechanical properties of  $\text{Si}_3\text{N}_4$  ceramic tool materials were improved by adding a new  $\text{TiC}_{0.7}\text{N}_{0.3}$  sintering aid to the traditional sintering additive combination of  $\text{Al}_2\text{O}_3$  and  $\text{Y}_2\text{O}_3$ . Using different sintering temperatures,  $\text{Si}_3\text{N}_4$  ceramic tool materials with excellent bending strength and fracture toughness were prepared. The relationship between the microstructure and mechanical properties of the prepared  $\text{Si}_3\text{N}_4$  ceramics was systematically characterized and discussed. Based on the experimental results and discussion, the following conclusions are drawn:

- (1) The added  $\text{TiC}_{0.7}\text{N}_{0.3}$  and the matrix  $\text{Si}_3\text{N}_4$  have different thermal expansion coefficients and elastic moduli; they prevent the growth of part of the grains so that the  $\beta$ - $\text{Si}_3\text{N}_4$  grains with different diameters and different aspect ratios are staggered and tightly combined with each other. At the same time, because  $\text{TiC}_{0.7}\text{N}_{0.3}$  has the characteristics of high hardness and high strength, it is uniformly dispersed in the matrix of  $\text{Si}_3\text{N}_4$  as a hard second phase, and the effect of strengthening and toughening is achieved. In addition, the effect of adding 1 vol%  $\text{TiC}_{0.7}\text{N}_{0.3}$  is relatively the best; the flexural strength and fracture toughness are 916 MPa and  $9.47 \text{ MPa}\cdot\text{m}^{1/2}$ , respectively.
- (2) Use of the Ostwald maturation mechanism to explain the grain growth process at different temperatures. By increasing the temperature of hot-pressing sintering, the degree of grain growth is greater, the degree of the interlacing of  $\beta$ - $\text{Si}_3\text{N}_4$  grains with different diameters and different aspect ratios is also gradually increased, and the mechanical properties of the material are also improved. The relative density, flexural strength, and fracture toughness reached 99.22%, 993 MPa, and  $9.81 \text{ MPa}\cdot\text{m}^{1/2}$ , respectively, when the hot-pressing sintering temperature was 1750 °C. However, there is still a great potential for improvement in numerical value.

**Author Contributions:** Conceptualization, S.G. and M.Z.; methodology, S.G. and F.Z.; validation, S.G., F.Z. and M.Z.; formal analysis, S.G., F.Z. and Z.X.; investigation, S.G.; resources, F.Z.; data curation, F.Z.; writing—original draft preparation, S.G.; writing—review and editing, X.S.; visualization, Z.X.; supervision, X.S. and M.Z.; project administration, X.S.; funding acquisition, M.Z. and X.S. All authors have read and agreed to the published version of the manuscript.

**Funding:** This research was funded by the National Natural Science Foundation of China (52072063, 51872033, 51732007) and a research start-up fund from the Foshan Graduate School of Innovation of Northeastern University.

**Institutional Review Board Statement:** Not applicable.

**Informed Consent Statement:** Not applicable.

**Data Availability Statement:** Not applicable.

**Conflicts of Interest:** The authors declare no conflict of interest.

## References

1. Tan, D.-W.; Zhu, L.-L.; Wei, W.-X.; Yu, J.-J.; Zhou, Y.-Z.; Guo, W.-M.; Lin, H.-T. Performance improvement of Si<sub>3</sub>N<sub>4</sub> ceramic cutting tools by tailoring of phase composition and microstructure. *Ceram. Int.* **2020**, *46*, 26182–26189. [\[CrossRef\]](#)
2. Souza, J.V.C.; Nono, M.C.A.; Ribeiro, M.V.; Machado, J.P.B.; Silva, O.M.M. Cutting forces in turning of gray cast iron using silicon nitride based cutting tool. *Mater. Des.* **2009**, *30*, 2715–2720. [\[CrossRef\]](#)
3. Lü, Z.; Deng, L.; Tian, Q.; Zhao, X. Cutting performance of Si<sub>3</sub>N<sub>4</sub>/TiC micro-nanocomposite ceramic tool in dry machining of hardened steel. *Int. J. Adv. Manuf. Technol.* **2017**, *95*, 3301–3307. [\[CrossRef\]](#)
4. Kwon, W.T.; Kim, Y.W. Cutting performance of Si<sub>3</sub>N<sub>4</sub> based SiC ceramic cutting tools. *KSME Int. J.* **2004**, *18*, 388–394. [\[CrossRef\]](#)
5. Zhao, J.; Yuan, X.; Zhou, Y. Cutting performance and failure mechanisms of an Al<sub>2</sub>O<sub>3</sub>/WC/TiC micro-nano-composite ceramic tool. *Int. J. Refract. Met. Hard Mater.* **2010**, *28*, 330–337. [\[CrossRef\]](#)
6. van Luttervelt, C.A.; Childs, T.H.C.; Jawahir, I.S.; Klocke, F.; Venuvinod, P.K.; Altintas, Y.; Armarego, E.; Dornfeld, D.; Grabec, I.; Leopold, J.; et al. Present Situation and Future Trends in Modelling of Machining Operations Progress Report of the CIRP Working Group ‘Modelling of Machining Operations’. *CIRP Ann.* **1998**, *47*, 587–626. [\[CrossRef\]](#)
7. Tu, L.; Tian, S.; Xu, F.; Wang, X.; Xu, C.; He, B.; Zuo, D.; Zhang, W. Cutting performance of cubic boron nitride-coated tools in dry turning of hardened ductile iron. *J. Manuf. Process.* **2020**, *56*, 158–168. [\[CrossRef\]](#)
8. Liu, W.; Chu, Q.; He, R.; Huang, M.; Wu, H.; Jiang, Q.; Chen, J.; Deng, X.; Wu, S. Preparation and properties of TiAlN coatings on silicon nitride ceramic cutting tools. *Ceram. Int.* **2018**, *44*, 2209–2215. [\[CrossRef\]](#)
9. Şap, S.; Usca, Ü.; Uzun, M.; Kuntoğlu, M.; Salur, E. Performance evaluation of AlTiN coated carbide tools during machining of ceramic reinforced Cu-based hybrid composites under cryogenic. *Pure-Minim. Quant. Lubr. Dry Regimes* **2022**, *56*, 3401–3421.
10. Xing, Y.; Deng, J.; Zhang, K.; Wang, X.; Lian, Y.; Zhou, Y. Fabrication and dry cutting performance of Si<sub>3</sub>N<sub>4</sub>/TiC ceramic tools reinforced with the PVD WS<sub>2</sub>/Zr soft-coatings. *Ceram. Int.* **2015**, *41*, 10261–10271. [\[CrossRef\]](#)
11. Mikolajczyk, T.; Paczkowski, T.; Kuntoglu, M.; Patange, A.; Binali, R. Research on Using an Unconventional Tool for Increasing Tool Life by Selective Exchange of Worn Cutting Edge. *Appl. Sci.* **2023**, *13*, 460. [\[CrossRef\]](#)
12. Wang, L.; Qi, Q.; Zhang, H.; Yang, X.; Liu, Z.; Ge, S.; Peng, X.; Liu, X.; Huang, Z. High tough W-added silicon nitride ceramics. *Ceram. Int.* **2019**, *45*, 19055–19059. [\[CrossRef\]](#)
13. Lucchini, E.; Lo Casto, S.; Sbaizero, O. The performance of molybdenum toughened alumina cutting tools in turning a particulate metal matrix composite. *Mater. Sci. Eng. A* **2003**, *357*, 369–375. [\[CrossRef\]](#)
14. Hu, Z.; Zhao, Z.; Deng, X.; Lu, Z.; Liu, J.; Qu, Z. Microstructure and mechanical behavior of TiCN reinforced AlSi<sub>10</sub>Mg composite fabricated by selective laser melting. *Mater. Chem. Phys.* **2022**, *283*, 125996. [\[CrossRef\]](#)
15. Yang, Y.; Dang, W.; Liu, J.; Zhang, H.; Gu, S.; Lei, C.; Chen, Y. Effect of the Addition of Ultrafine Powders on the Microstructure and Mechanical Properties of TiCN-Based Cermets. *J. Ceram. Sci. Technol.* **2022**, *13*, 15–22.
16. Meng, J.; Lu, J.; Wang, J.; Yang, S. Tribological behavior of TiCN-based cermets at elevated temperatures. *Mater. Sci. Eng. A* **2006**, *418*, 68–76. [\[CrossRef\]](#)
17. Wang, B.; Liu, Z. Cutting performance of solid ceramic end milling tools in machining hardened AISI H13 steel. *Int. J. Refract. Met. Hard Mater.* **2016**, *55*, 24–32. [\[CrossRef\]](#)
18. Xiong, H.; Wen, Y.; Gan, X.; Li, Z.; Chai, L. Influence of coarse TiCN content on the morphology and mechanical properties of ultrafine TiCN-based cermets. *Mater. Sci. Eng. A* **2017**, *682*, 648–655. [\[CrossRef\]](#)
19. Lee, B.T.; Yoon, Y.J.; Lee, K.H. Microstructural characterization of electroconductive Si<sub>3</sub>N<sub>4</sub>-TiN composites. *Mater. Lett.* **2001**, *47*, 71–76. [\[CrossRef\]](#)
20. Kgoete, F.M.; Popoola, A.P.I.; Fayomi, O.S.I.; Adebisi, I.D. Spark plasma sintered Ti-6Al-4V-Si<sub>3</sub>N<sub>4</sub>-TiN ternary composites: Effect of combined micro-sized Si<sub>3</sub>N<sub>4</sub> and TiN addition on microstructure and mechanical properties for aerospace application. *J. Alloys Compd.* **2018**, *769*, 817–823. [\[CrossRef\]](#)

21. Huang, J.L.; Chang, Y.L.; Lu, H.H. Fabrication of multilaminated Si<sub>3</sub>N<sub>4</sub>-Si<sub>3</sub>N<sub>4</sub>/TiN composites and its anisotropic fracture behavior. *J. Mater. Res.* **1997**, *12*, 2337–2344. [[CrossRef](#)]
22. Miyazaki, H.; Hyuga, H.; Yoshizawa, Y.-I.; Hirao, K.; Ohji, T. Correlation of wear behavior and indentation fracture resistance in silicon nitride ceramics hot-pressed with alumina and yttria. *J. Eur. Ceram. Soc.* **2009**, *29*, 1535–1542. [[CrossRef](#)]
23. Tsuge, A.; Nishida, K.; Komatsu, M. Effect of Crystallizing the Grain-Boundary Glass Phase on the High-Temperature Strength of Hot-Pressed Si<sub>3</sub>N<sub>4</sub> Containing Y<sub>2</sub>O<sub>3</sub>. *J. Am. Ceram. Soc.* **1975**, *58*, 323–326. [[CrossRef](#)]
24. Zhu, X.; Sakka, Y. Textured silicon nitride: Processing and anisotropic properties. *Sci. Technol. Adv. Mater.* **2008**, *9*, 033001. [[CrossRef](#)]
25. Hampshire, S. Silicon nitride ceramics—Review of structure, processing and properties. *J. Achiev. Mater. Manuf. Eng.* **2007**, *24*, 43–50.
26. Liao, S.; Zhou, L.; Jiang, C.; Wang, J.; Zhuang, Y.; Li, S. Thermal conductivity and mechanical properties of Si<sub>3</sub>N<sub>4</sub> ceramics with binary fluoride sintering additives. *J. Eur. Ceram. Soc.* **2021**, *41*, 6971–6982. [[CrossRef](#)]
27. Cinibulk, M.K.; Thomas, G.; Johnson, S.M. Fabrication and Secondary-Phase Crystallization of Rare-Earth Disilicate-Silicon Nitride Ceramics. *J. Am. Ceram. Soc.* **1992**, *75*, 2037–2043. [[CrossRef](#)]
28. Shen, Z.; Zhao, Z.; Peng, H.; Nygren, M. Formation of tough interlocking microstructures in silicon nitride ceramics by dynamic ripening. *Nature* **2002**, *417*, 266–269. [[CrossRef](#)]
29. Xiong, J.; Guo, Z.; Wen, B.; Li, C.; Shen, B. Microstructure and properties of ultra-fine TiC<sub>0.7</sub>N<sub>0.3</sub> cermet. *Mater. Sci. Eng. A* **2006**, *416*, 51–58. [[CrossRef](#)]
30. Gao, J.; Song, J.; Lv, M.; Cao, L.; Xie, J. Microstructure and mechanical properties of TiC<sub>0.7</sub>N<sub>0.3</sub>-HfC cermet tool materials. *Ceram. Int.* **2018**, *44*, 17895–17904. [[CrossRef](#)]
31. Wang, B.; Yang, J.; Guo, R.; Gao, J.-Q.; Yang, J.-F. Microstructure characterization of hot-pressed β-silicon nitride containing β-Si<sub>3</sub>N<sub>4</sub> seeds. *Mater. Charact.* **2009**, *60*, 894–899. [[CrossRef](#)]
32. Dai, J.; Li, J.; Chen, Y.; Yang, L. Effect of the residual phases in β-Si<sub>3</sub>N<sub>4</sub> seed on the mechanical properties of self-reinforced Si<sub>3</sub>N<sub>4</sub> ceramics. *J. Eur. Ceram. Soc.* **2003**, *23*, 1543–1547. [[CrossRef](#)]
33. Perera, D.S.; Mitchell, D.R.G.; Leung, S. High aspect ratio β-Si<sub>3</sub>N<sub>4</sub> grain growth. *J. Eur. Ceram. Soc.* **2000**, *20*, 789–794. [[CrossRef](#)]
34. Hirosaki, N.; Okamoto, Y.; Munakata, F.; Akimune, Y. Effect of seeding on the thermal conductivity of self-reinforced silicon nitride. *J. Eur. Ceram. Soc.* **1999**, *19*, 2183–2187. [[CrossRef](#)]
35. Hu, J.; Zhang, B.; Li, C.; Wang, L.; Wang, S.; Shi, Z.; Yang, J. Fabrication of Si<sub>3</sub>N<sub>4</sub> ceramics with high thermal conductivity and flexural strength via novel two-step gas-pressure sintering. *J. Eur. Ceram. Soc.* **2022**, *42*, 4846–4854. [[CrossRef](#)]
36. Deeley, G.G.; Herbert, J.M.; Moore, N.C. Dense Silicon Nitride. *Powder Metall.* **1961**, *4*, 145–151. [[CrossRef](#)]
37. German, R.M. Coarsening in Sintering: Grain Shape Distribution, Grain Size Distribution, and Grain Growth Kinetics in Solid-Pore Systems. *Crit. Rev. Solid State Mater. Sci.* **2010**, *35*, 263–305. [[CrossRef](#)]
38. Hirao, K.; Watari, K.; Hayashi, H.; Kitayama, M. High Thermal Conductivity Silicon Nitride Ceramic. *MRS Bull.* **2001**, *26*, 451–455. [[CrossRef](#)]

**Disclaimer/Publisher’s Note:** The statements, opinions and data contained in all publications are solely those of the individual author(s) and contributor(s) and not of MDPI and/or the editor(s). MDPI and/or the editor(s) disclaim responsibility for any injury to people or property resulting from any ideas, methods, instructions or products referred to in the content.